SOHO/CDS and Ground Based Observations of a Two-Ribbon Flare: Spatially Resolved Signatures of Chromospheric Evaporation

L. Teriaca, A. Falchi and G. Cauzzi

INAF-Osservatorio Astrofisico di Arcetri, Largo Enrico Fermi 5, 50125 Firenze, Italy

lte@arcetri.astro.it

R. Falciani

Dipartimento di Astronomia e Scienza dello Spazio, Università di Firenze, Largo Fermi 5, 50125 Firenze, Italy

L. A. Smaldone

Dipartimento di Scienze Fisiche, Università di Napoli "Federico II", 80126 Napoli, Italy

and

V. Andretta

INAF-Osservatorio Astronomico di Capodimonte, Via Moiariello 16, 80131 Napoli, Italy

ABSTRACT

During a coordinated observing campaign (SOHO JOP 139), we obtained simultaneous spectroheliograms of a solar active region in several spectral lines, sampling levels from the chromosphere to the corona. Ground based spectroheliograms were acquired at the Dunn Solar Tower of NSO/Sacramento Peak in four chromospheric lines, while the Coronal Diagnostic Spectrograph (CDS) aboard SOHO was used to obtain rasters of the active region in transition region (TR) and coronal lines. Such a complete dataset allowed us to compare the development of intensity and velocity fields during a small two-ribbon flare in the whole atmosphere. In particular, we obtained for the first time quasi-simultaneous and spatially resolved observations of velocity fields during the impulsive phase of a flare, both in chromosphere and upper atmosphere. In this phase, strong downflows (up to 40 km s^{-1}) following the shape of the developing ribbons are measured at chromospheric levels, while strong upward motions are instead measured in TR (up to -100 km s^{-1}) and coronal lines (-160 km s^{-1}). The spatial

pattern of these velocities have a common area about 10 arcsec wide. This is the first time that opposite directed flows at different atmospheric levels are observed in the same spatial location during a flare. These signatures are highly suggestive of the chromospheric evaporation scenario predicted in theoretical models of flares.

Subject headings: Sun: activity — Sun: flares — Sun: atmospheric motions

1. INTRODUCTION

Plasma motions have long been observed during the impulsive phase of a flare both at coronal and at chromospheric levels. Blue-shifted emission in the Ca XIX, S XV and Fe XXV coronal lines (Doschek et al. 1980; Antonucci et al. 1982) and red-shifted emission in Hα, other Balmer lines and Ca II K (Ichimoto & Kurokawa 1984; Falchi, Falciani, & Smaldone 1992; Wülser et al. 1994;) has been observed to peak simultaneously with microwave and hard X-ray bursts. These shifts have been interpreted respectively as coronal up-flows with velocities up to 400 km s^{-1}, and chromospheric down-flows with velocities up to 100 km s^{-1}, and can be explained through hydrodynamic simulations. From the years 1980s onward, models of flares have in fact stressed the relevance of the so-called "explosive chromospheric evaporation", a sudden increase of the chromospheric temperature to coronal values, occurring when the chromospheric plasma is heated beyond its ability to radiate. The overpressure of this gas drives material both upward (at coronal levels) and downward (at chromospheric levels) simultaneously with hard X-ray bursts (Nagai & Emslie 1984; Fisher 1986; Gan, Zhang, & Fang 1991).

Since the overpressure of the chromospheric evaporated gas is responsible for the dynamics of the flare, the momentum of downward moving chromospheric plasma (observed for example in Hα) should be equal to the momentum of the ablating plasma as revealed by the blue-shifted emission in coronal lines. The equality of the two momenta has been proved within a factor of 2-6, consistent with uncertainties of the measurements, only for a few events for which simultaneous chromospheric and coronal observations were available during the impulsive phase (Zarro et al. 1988; Canfield et al. 1990; Wülser, Zarro & Canfield 1992). It must be noted that in these cases the coronal observations were spatially unresolved, and hence the location of the blue-shifted plasma has been assumed to be the same of the red shifted chromospheric material. The only indirect observational proof that both coronal upflows and chromospheric downflows originate in the same spatial location has been provided by Wülser et al. (1994). They show that the kernels of chromospheric downflows spatially coincide with the soft X-ray loop footpoints, presumably the loci of energy deposition and

hence of coronal upflows. Also for this flare the upward and downward momenta, originating in the same locations, coincide within the errors. (cf. review by Culhane 1996).

New instruments such as the Coronal Diagnostic Spectrometer (CDS; Harrison et al. 1995, 1997) aboard SOHO, that provide both spectral and spatial information, offer new insights into this problem. Spatially resolved observations of the late gradual phase of a large two-ribbon flare have been obtained by Czaykowska et al. (1999) using CDS data. They observe blueshifts in spectral lines of O V, Fe XVI and Fe XIX, located only in the outmost region of the Hα ribbons, and interpret such signatures as evidence of chromospheric evaporation for ongoing magnetic reconnection. Moderate upflows have been observed also by Del Zanna et al. (2002) in coronal lines such as Mg X and Si XII during the development of a small flare. However, spatially resolved and simultaneous observations of flows in chromospheric and upper atmospheric layers during the development of a flare, particularly during its impulsive phase, are still lacking.

We contribute to this topic presenting here observations of a small two-ribbon flare (GOES class C1.1), developing in region NOAA 9468 on May 26, 2001 around 16 UT (cosθ=0.99). During a coordinated campaign (SOHO JOP 139), we obtained simultaneous spectroheliograms of the same area in several spectral lines, from the chromosphere to the corona, that allow us to compare the development of the flare intensity and velocity in the whole atmosphere. Although the program was originally meant to study the evolution of He abundances in active regions and flares, and thus was not optimized in terms of temporal resolution, we obtained a fairly complete coverage of the temporal evolution of the flare, from the pre-flare through impulsive to decay phase. In Section 2 we describe the observations. Section 3 outlines the morphology of the flare evolution, while Section 4 and Section 5 describe the flare intensity and velocity signatures, respectively. Finally, Section 6 concludes the paper.

2. OBSERVATIONS

2.1. CDS Data

The Coronal Diagnostic Spectrometer feeds simultaneously a Normal Incidence Spectrometer (NIS) and a Grazing Incidence Spectrometer (GIS). NIS spectra were acquired exposing the detector for 8 s through the $4'' \times 240''$ slit. After each exposure the slit was moved $6''$ eastward covering a $148''$ wide area in ~ 5.5 minutes (24 steps). Due to telemetry constraints only 88 pixels along the slit were binned over two and transmitted to the ground, yielding a final spatial resolution of $6'' \times 3.4''$. This leads to an undersampling of the solar

surface. Measured line radiances give the average energy per time and solid angle emitted by the unit area of the region on the solar surface covered by the CDS resolution element (in this case $4'' \times 3.4''$). Here we assume that this value is equal to that related to the wider $6'' \times 3.4''$ effective resolution element of our data. The final useful FOV was $148'' \times 138''$. Every eleven raster scans the raster starting position was shifted to compensate the solar rotation. In such a way, spectroheliograms of the active region were obtained in five spectral windows around the He I 584 (log T=4.3), He II 304 (log T=4.8), O V 630 (log T=5.4), Fe XVI 360 (log T=6.3), and Fe XIX 592 Å (log T=6.9) spectral lines. The atmospheric heights sampled by these lines span from the high chromosphere, through the transition region (TR), to the corona.

2.2. Ground Based Data

Spectroheliograms were acquired with the Horizontal SpectroGraph (HSG) at the Dunn Solar Telescope (DST) of the National Solar Observatory / Sacramento Peak in the chromospheric lines Ca II K, Hα, He I 5876 Å (D3) and He I 10830 Å. The formation mechanism of these two He I lines is normally due to scattering of photospheric radiation by helium atoms in the 1s2s ^{3}S and 1s2p ^{3}P triplet states. These excited states are populated mostly in the upper layers of the solar atmosphere, either in the chromosphere or in the lower TR, or in both.

The chromospheric contribution, due to recombination cascades following photoionization by UV (mostly coronal) radiation, is always present in the quiet Sun or in active regions (e.g. Fontenla, Avrett, & Loeser, 1993). On the other hand, the importance of the lower TR contribution, due to direct collisional excitation, possibly enhanced by non-thermal processes, is still largely debated (Andretta & Jones, 1997). Preliminary modeling of these data (P. Mauas 2002, private communication), including non-thermal effects such as ambipolar diffusion, seems to indicate that in the case of our observations, the TR has little effect on the strength of the optical He I triplet lines.

There is little doubt, instead, that the TR contribution is important in the formation of the He I 584 Å resonance line (Andretta & Jones, 1997; Andretta, Del Zanna, & Jordan, 2002). Thus, the He I 584 Å line, as well as the other He I and He II resonance UV lines, are sensitive to higher layers than the He I 10830 Å and He I D_3 lines. In terms of formation height, a parallel can be drawn with, respectively, the hydrogen Lyα and Hα lines: the latter is the quintessential chromospheric line, while the former has much in common with TR lines. Such a scenario is consistent with the characteristics of the intensities and velocities observed in our data, as described in Sections 4 and 5.

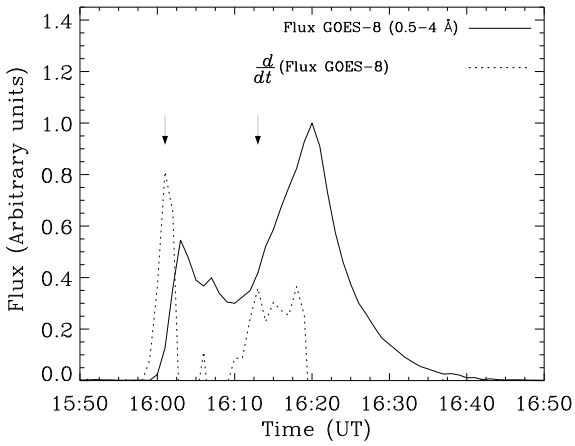

Fig. 1.— Soft X-ray full disk flux at 1 AU in the 0.5−4 Å band (solid line) around the time of the flare (GOES-8 data). The time derivative (dotted line) represents a proxy for the hard X-ray curve. Main local maxima in the derivative ($\sim 16:01$ and $\sim 16:13$ UT) are marked by arrows.

The full field of view of the DST, $170'' \times 170''$, was covered in about 5 minutes, with a sampling step of $2''$ (from east to west, i.e. opposite to the CDS sampling direction). The final spatial scale along the slit was set to $2''$. Correcting for offsets among the different detectors resulted in a final useful FOV of $160'' \times 140''$, slightly shifted westward with respect to the one observed with CDS (see Fig. 3).

Sequences of spectroheliograms were taken without interruption during the interval of coordinated space observations. During this time, the solar rotation was continuously tracked by the telescope.

Finally, images at several wavelengths within the Hα line and the continuum were acquired on the same FOV by means of the Universal Birefringent Filter (UBF), with a spatial scale of $1'' \times 1''$ and few s temporal cadence. Unfortunately a misfunctioning of the system prevented a correct acquisition, so that only some of these images could be exploited.

2.3. Support Data

A measure of the soft X-ray flux in the 0.5 - 4 Å and 1 - 8 Å ranges was provided by the GOES-8 and GOES-10 satellites. The 0.5 - 4 Å flux around the time of the flare development is displayed in Figure 1, together with its temporal derivative. As discussed in

Dennis & Zarro (1993), in about 80% of the flares the time derivative of the GOES curve well agrees with the temporal evolution of the hard X-ray curve (Neupert effect; Neupert, 1968). Recently Veronig et al. (2002), using a much larger sample, find a similar result, with only 25% of flares showing strong deviations from the timing expectations of the Neupert effect. Since no hard X-ray (HXR) measurement was available for the flare here analyzed, we used the time-derivative of the SXR flux as a proxy for the HXR emission (see next Sections). Two main bursts in the derivative are visible at $\sim$ 16:01 and $\sim$ 16:13 UT, with the first one much more abrupt and intense than the second one, although the global SXR emission peaks only at 16:20 UT.

A full disk longitudinal magnetogram was obtained by MDI (Scherrer et al. 1995) on SOHO at 16:00 UT, and was used to define the magnetic neutral line shown in figures throughout the paper. MDI also provided images of the Sun in the optical continuum around 6800 Å that have been used to coalign the data (see below).

2.4. Alignment

Final ground-based and CDS data were aligned using MDI as a reference. First, rasters in the continuum around Hα were aligned with MDI continuum images, providing a good registration between chromospheric data and magnetograms. We estimate the error around $1''$. A comparison between spectroheliograms in He I 584 and Hα, that display very similar features, provided the alignment between CDS and ground based data, within a few arcseconds.

Due to the acquisition process, CDS and ground based spectra are not strictly simultaneous, with time lags depending on time and X position on the FOV. Each spectrum was, hence, tagged with its own acquisition time so that light and velocity curves derived from different instruments could be properly compared. Times of Hα spectroheliograms given throughout this paper refer to the moments in which slits crossed position X= $-30''$, roughly corresponding to the position of the first flaring kernel.

3. Hα FLARE DEVELOPMENT

Although very small in the GOES soft-X ray classification (C1.1) the flare under study displays all the characteristics of an eruptive flare. Its evolution is summarized by the sequence of Hα images, obtained with the UBF, displayed in Figure 2.

First, a thin filament was visible within the active region (Fig. 2*a*), following very closely

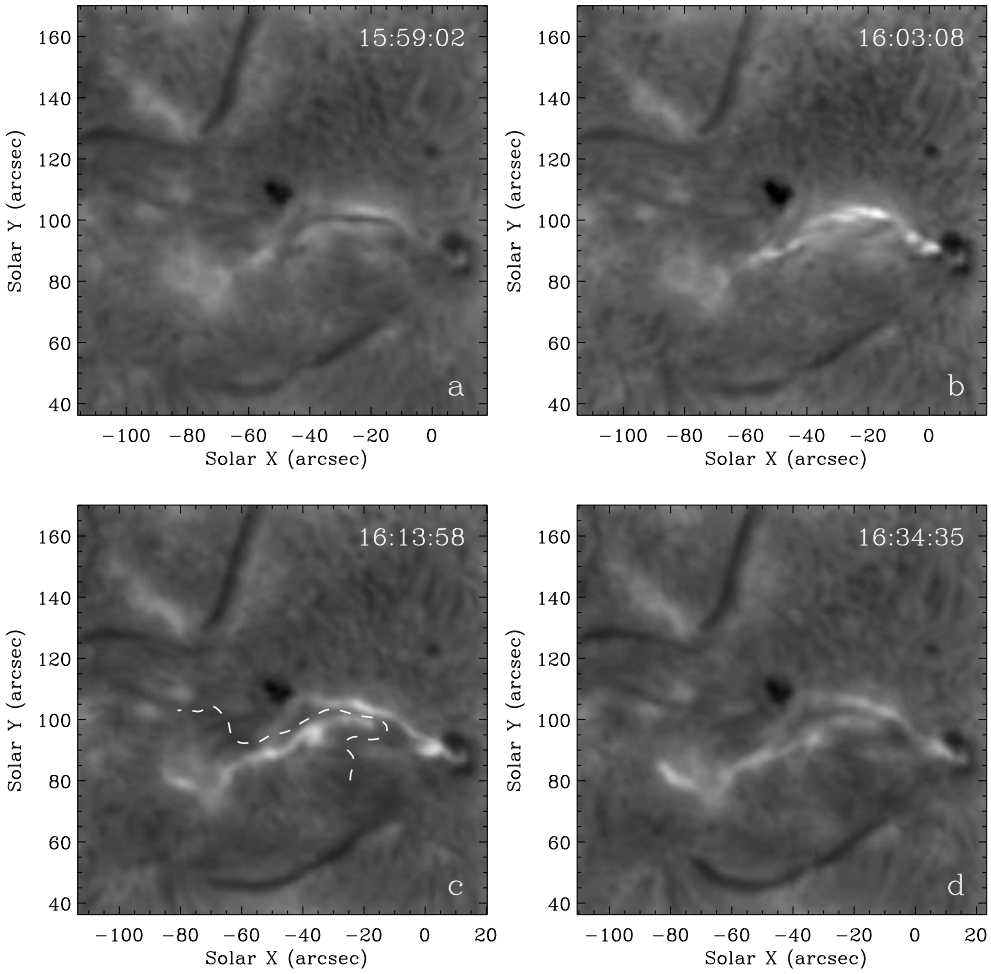

Fig. 2.— UBF Hα images summarizing the flare evolution. X direction is parallel to the solar equator. The images are displayed on the same scale, to show the relative brightenings.*(a)* Pre-flare phase. At this time, the filament within the active region is thickening and undergoing upward motions. *(b)* First phase of ribbon development. *(c)* Second major energy release episode. Different bright ribbon kernels are visible. The dashed line represents the magnetic inversion line derived from MDI data acquired at 16:00 UT. *(d)* Decay phase. New, less intense kernels develop further away from the neutral line.

the upper-right portion of the magnetic neutral line outlined in Figure 2*c*. The filament itself, and the further flare development suggest the presence of an arcade of low-lying, sheared magnetic loops connecting opposite polarities. We remark here that while the large filaments present in the N-E and S-W quadrants of the FOV are well detectable as dark features in the O V and He I 584 Å spectroheliograms, the thin active region filament is not visible in

CDS data at any time, either due to its very small extension in the Y-direction with respect to the CDS spatial resolution, or to its limited height. Few minutes before the start of the flare (as defined by the first Neupert peak, 16:01 UT), the filament thickened and erupted at its western-most end (roughly between X= $-30''$ and X=$-15''$ in Fig. 2*a*). The eruption is visible both as a darkening of the filament in the UBF Hα blue-wing images, and as upward motions measured in the chromospheric lines (see Sect. 5.2). Being at disk center, we didn't observe any obvious displacement in height of the filament itself.

Two flare ribbons then rapidly developed on either side of the magnetic neutral line (Fig. 2*b*). At the time of this Figure (about two minutes after the first Neupert peak) the ribbons are still very close to the magnetic neutral line.

A second major episode of energy release occurred around 16:13 UT, as indicated by the second peak in the time derivative of the SXR curve (Fig. 1). At both chromospheric and TR level, this phase is characterized by the brightening of different kernels in the flaring ribbons. The ribbons are expanding farther away from the magnetic neutral line and appear now clearly separated (Fig. 2*c*).

As typical of eruptive flares, the decay phase extended for a fairly long period (more than 40 minutes from the second soft X-ray peak, see Fig. 1), with successive episodes of energy release that affected portions of the ribbons farther away from the neutral line (Fig. 2*d*). From the beginning of the impulsive phase, and for about 30 minutes, the filament was not visible in the Hα images, as the magnetic polarity inversion line is wholly embedded in the flare. Once it became visible again in the late flare phase (Fig. 2*d*), it appeared in the same position and with roughly the same shape as in the pre-flare phase. The thickening and upward motions witnessed around 15:59 UT (Fig. 2*a*) hence might have affected only an upper layer of the filament, much as the cases described in Tang (1986). We will discuss the issue further in Section 6.

4. INTENSITY EVOLUTION

Figure 3 shows spectroheliograms in Hα center, with overlaid radiance contours for the spectral lines observed with CDS. He II data are not reported in Figure since they basically confirm the He I 584 behavior. The magnetic inversion line derived from MDI is again indicated with a dashed white line. Top panels show the time of the first "Neupert" peak (around 16:01 UT), and bottom panels the time closest to the second "Neupert" peak (around 16:13 UT).

A few comments are in order on this figure. First, from the left-side panels it is evident

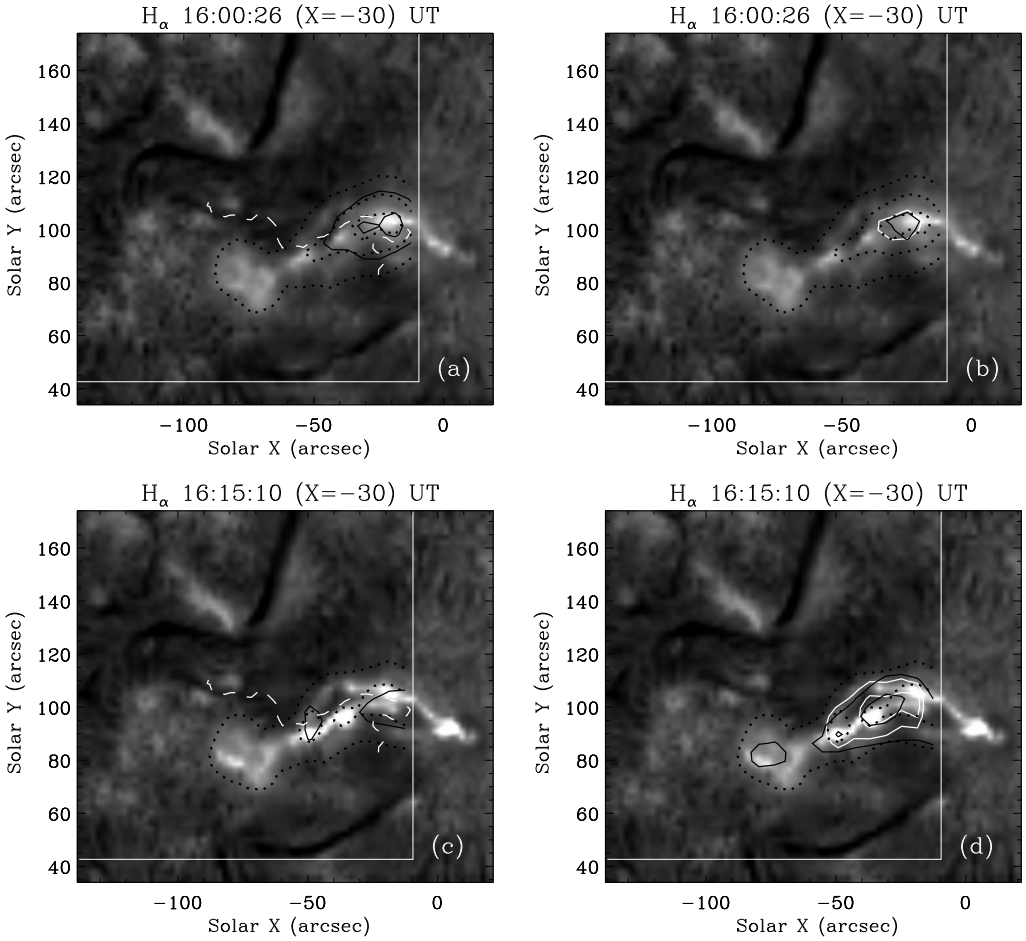

Fig. 3.— Hα spectroheliograms with overlaid CDS radiance contours. In all panels, black dotted lines indicate radiance levels of 12, 35 and 96 W m^{-2} sr^{-1} for the He I 584 Å line. Note that only the two lower levels are visible on panels *(c, d)*. On the left panels *(a, c)*, black solid lines show O V radiance isocontours of 10 and 60 W m^{-2} sr^{-1} (only the lower level is visible on panel *(c)*. On the right panels *(b, d)*, white solid lines mark radiance levels of 8.5 and 12 W m^{-2} sr^{-1} for Fe XVI while, for the Fe XIX, black solid lines indicate levels of 0.13 and 0.49 W m^{-2} sr^{-1}. Note that, for the two high temperature Iron lines, only the lower radiance level is visible on panel *(b)*, with a temporal behaviour opposite to that of the TR lines. The white dashed line on panels *(a)* and *(c)* marks the position of the magnetic neutral line. The thin white lines indicate the limits of the CDS field of view.

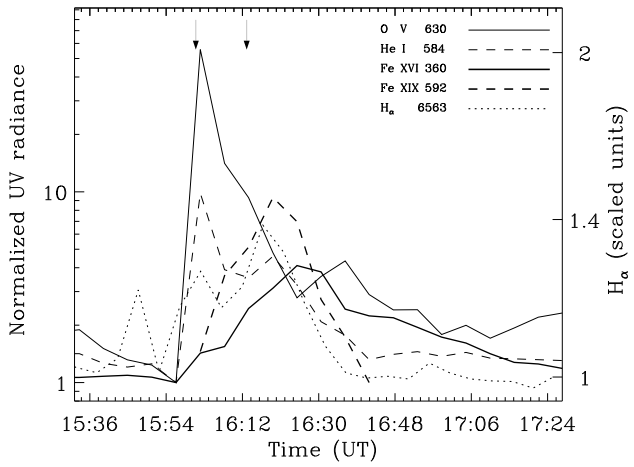

Fig. 4.— Light curves at the location of maximum O V brightening ($-20''$, $100''$). O V, He I, and Fe XVI light curves are normalized to the value measured at 15:57 UT, before the flare onset. Fe XIX light curve is normalized to the value measured around 16:42 UT (last spectrum in which Fe XIX emission was still detectable). Hα light curve is scaled for displaying purposes, having only a $\sim 40\%$ variation between the pre-event and the maximum values. Arrows correspond to the time positions of the main peaks in the time derivative of the SXR curve (see Fig. 1).

that the emission of lines formed at high chromosphere and TR temperatures maps very well the spatial distribution of the Hα intensity, i.e. the TR kernels coincide with the chromospheric footpoints of the flaring loops. The maximum radiance in both O V and He I 584 occurs during the earliest phase of the flare (16:02 UT in CDS data), and corresponds roughly to 60 and 10 times the radiance measured at the same location ($-20''$, $100''$) at 15:57 UT, respectively. Both UV lines decrease with time (see also Fig. 4), but still outline well the chromospheric flaring areas even during the second episode of energy release. In particular, in Figure 3*c* one can notice a new and very localized kernel around position ($-50''$, $90''$) visible in all signatures.

From the right-hand panels of Figure 3, one can see indeed that the maximum coronal emission is located between the ribbons. Moreover, both the area and intensity of the coronal emission slowly increase with time, reaching their peaks around 16:20 UT (see Fig. 4), i.e. the time of the second GOES maximum. Maximum radiance values for Fe XVI are of the order of 4 times that measured at the same location at 15:57 UT, while Fe XIX is not present at pre-flare times.

The intensity evolution during the flare at the region of maximum O V brightening is

further described with the light curves of Figure 4. TR light curves show a strong peak related to the first brightenings observed at chromospheric levels (around 16:01 UT), while coronal lines show a more gradual increase peaking around 16:20 UT, at the maximum of the SXR light curve (see Fig. 1). O V, He I, and Fe XVI light curves are normalized to the pre-flare value. Fe XIX light curve is normalized to the value measured in the last spectrum in which Fe XIX emission was still detectable (around 16:42 UT)

Light curves confirm the impulsive behavior of the TR lines emission, especially that of O V. The first flaring episode is clearly seen in both O V and He I lines. The second flaring episode is seen as a separate peak in the Hα and in the He I curves, while it is visible only as a "shoulder" in the O V curve during the decay phase of the first burst. In general, the evolution of the He I line radiance closely follow that of the Hα line. The coronal lines emission show instead a slow and steady increase after the beginning of the flare, and reach their maximum only later, several minutes after the second Neupert peak.

All of this is consistent with previous observations showing that the O V emission during a flare is due to small and very localized areas of high densities (Cheng 1984) and has a very impulsive behaviour, following the trend of the HXR emission not only in the impulsive phase but also during secondary peaks (Woodgate et al. 1983; Cheng et al. 1988). The data seem to validate the idea that the flare energy is released impulsively in the corona and transported by accelerated non-thermal electrons or by thermal conduction to the loop footpoints. The heated chromospheric material then flows up into the loop and produces the gradually rising soft X-ray signal.

5. VELOCITY EVOLUTION

Mass motions during flares have been extensively studied in the corona and chromosphere, but only few measurements of velocities in the transition region are available, mostly obtained with older instruments aboard SMM and OSO-8. Mostly red-shifted emission, interpreted as downflows of 30-80 km s^{-1}, is reported in TR flare spectra. Cheng & Tandberg-Hanssen (1986) found that these downflows are correlated, temporally and spatially, with maximum intensity of the studied Si IV line, while Lites, Bruner, & Wolfson (1981) found them to precede the impulsive brightening of C IV. It must be noted, however, that in both cases line profiles were acquired by means of a sequential wavelength scanning (30-150 s scanning time). Given the very impulsive response of TR lines in flares, this could represent a serious limitation to the determination of velocity. From spatially unresolved SOLSTICE observations, Brekke et al. (1996) found downflows of about 50 km s^{-1} in TR lines during the impulsive phase of one single flare. These motions are interpreted as due to a compression

of the original transition region into deeper atmosphere during the flare bursts.

Blue-shifts, interpreted as upflows at TR levels, are occasionally reported as well by the same authors. In particular, Lites et al. (1981) ascribe to chromospheric evaporation the small upflow (-10 km s^{-1}) observed simultaneously to maximum brightening of C IV in one case. Finally, Czaykowska et al. (1999) report of small upflows (~ -20 km s^{-1}) measured in O V only in the outer portions of the flare ribbons during the decay phase. Again, such flows are interpreted as evidence of on-going chromospheric evaporation.

The panorama of flows in TR during flares is hence somewhat confused, both for a real lack of data, and for the limitations suffered by the available observations. Our dataset combines spatially resolved spectral observations with quasi-simultaneously measurements in the chromosphere and the upper atmospheric layers, and hence seems particularly suitable to shed some light on the problem. The procedures adopted to recover velocities with the different lines are explained in some detail in the next subsection. We proceed then to describe the flows developing during the flare. We remark that AR 9468 was located very near disk center, i.e. there is no ambiguity in the recovered direction of the flows.

5.1. Measurements of Flows

Measurement of flows requires very careful line profile and position estimates; hence, we briefly present here important steps in their determination.

Chromospheric lines. As described in Section 2.2, we obtained spectra around four chromospheric lines: Ca II K, Hα, He I 5876 and He I 10830 Å. Because of their sensitivity to UV coronal radiation, these He I lines in active regions and flares have a strong contribution from high chromospheric layers. Hence, these lines respond, if not totally, at least in part to the same layers as Hα. Flows measured in these three lines in fact agree quite well both in spatial distribution and velocity amplitudes. On the other hand, the Ca II K line shows a surprising lack of signatures of flows during the flare. From preliminary models of the pre-flaring atmosphere, we concluded that in this small flare the Ca II K line samples atmospheric layers around 1000 km deeper than the other lines (P. Mauas 2002, private communication), only marginally affected by the flare. In the following we will refer only to flows measured in He I 10830.

We show in Figure 5*a* the He I 10830 profile averaged on the active region before the flare start (thin line) and in the flaring point where maximum upward velocities are measured in O V (thick line). The flare line, although still in absorption, is much stronger than the quiet case, and clearly shows a red-shifted component. The Doppler shifts were measured using a

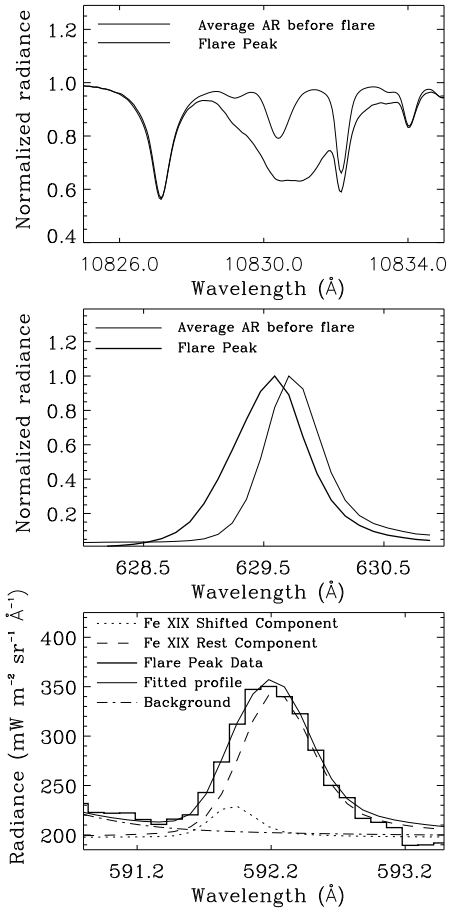

Fig. 5.— He I 10830, O V 630 and Fe XIX 592 Å line profiles observed during the flare peak (thick solid lines) in the location of maximum O V blueshift (X= $-37''$, Y= 101). Strong red-shifts are visible in the chromospheric line while blue-shifts characterize the TR and coronal lines. *(a)* Average He I 10830 active region line profile before flare (thin solid line) together with the flare profile. *(b)* Normalized O V flare line profile together with the line profile obtained averaging the whole last scan taken before the flare (thin solid line). *(c)* Fe XIX flare profile (thick solid histogram) together with the fitted spectral profile (thin solid line). The Fe XIX rest component is indicated with a thin dashed line, while the thin dotted line shows the blueshifted component. A thin dot-dashed line marks the fitted background.

multi-Gaussian fit to the profiles, fixing the rest wavelength and width of the two reference lines at 10827 and 10832 Å. Errors have been evaluated from the residuals of the fit, and amount to ± 10%.

CDS lines. Since spectra acquired after recovery of the SOHO spacecraft are character-

ized by very broad and asymmetric profiles, we had to fit each line profile with an opportune template provided within the CDS software. We remark that the broad instrumental profile prevents a quantitative estimate of the line widths and hence, of the possible turbulent velocity components during the flare.

Flows in He I 584, and O V 630 Å lines have been computed fitting a single component to the line profiles. Since these lines have an obvious pre-flare component, a reference wavelength has been obtained averaging the central positions derived from the fitting for the whole dataset. No drifts and/or systematic errors have been revealed across the dataset. Velocities have then been computed simply using the Doppler-shift of the flare profiles with respect to the reference wavelength. In Figure 5*b* we show the O V profile from which maximum upward velocity (~ -100 km s^{-1}) is measured at 16:02:30 UT (thick solid line) around X= $-37''$, Y= $101''$, together with the profile obtained averaging the entire scan preceding the flare onset (thin solid line). A double component fitting was also applied to the flare profile in Figure 5*b*, constraining width and position of the rest component through the average profile before the flare. This analysis yields a blueshift of ~ -125 km s^{-1}, not significantly different from that obtained adopting a single component fitting. He I 584, He II 304 and O V 630 provide essentially the same information, although the amplitude of the flows is lower in the He lines. Errors on best-fit parameters are evaluated accounting for data noise (photon statistics, pulse height distribution and readout noise) and the adopted 3-σ error amount to 15−18 km s^{-1} over the active region.

The measure of flows in the hot ($\log T = 6.9$ K) Fe XIX 592 line requires a more careful analysis. Since the line appears only during flares, one has to exercise great caution in choosing the reference profile. [1] Profiles significantly diverging from the reference profile are visible only at 16:02 UT around the location of maximum O V blue-shifts. Due to the very weak emission of the Fe XIX line at flare onset (see Fig. 4), we found it necessary to average over 5 CDS pixels in order to improve the S/N ratio. These are the pixels with upward velocities larger than ~ -80 km s^{-1} in O V. The obtained profile is shown as thick solid histogram in Fig. 5*c*. The line profiles obtained averaging over the same CDS points at the four successive scans (from 16:08:14 to 16:25:21 UT) are instead identical in width and position and their average was used as a reference profile (thin dashed line in Fig. 5*c*). Note that the red wing of the profile at flare onset is identical to that of the reference

[1]The average spectrum within the active region, before and after the flare occurrence and the average spectrum outside the AR are very similar and both show a weak line whose central wavelength is shifted by more than 0.4 Å redward from the nominal Fe XIX rest position. This line cannot be due to Fe XIX, but rather to an unidentified line observed in second order (a Si IX line around 296.3 Å is given by Mason & Bhatia 1977). See also Fig. 5 in Del Zanna et al. 2002.

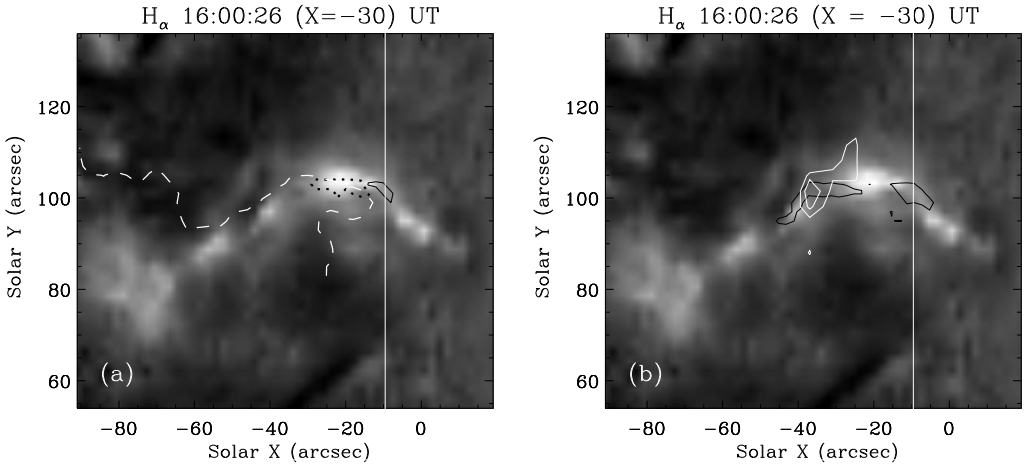

Fig. 6.— *(a)*: Velocity contours for He I 10830 around 16:00:26 UT (−20 km s^{-1} – black dotted lines and 20 km s^{-1} – black solid lines. Upward is negative). The background Hα image is simultaneous to the He I 10830 measurements. The blueshifted pattern betrays the filament eruption before the flare. *(b)*: Contours of He I 10830 downflows measured around 16:05:14 UT (+25 km s^{-1}, black solid lines), overlaid on the same image of panel *a*. Isocontours of the velocities measured around 16:02 UT with the O V 630 (−80, −60 km s^{-1} – white solid line) are also shown.

profile, while an enhanced blue wing is clearly visible. A multi component fitting was hence applied to the 16:02 UT profile, constraining the rest component by imposing width and position of the reference profile, while the background (thin dot-dashed line in Fig. 5*c*) was constrained through the average non-flare spectrum. A blue-shifted component (thin dotted line in Fig. 5*c*) is now evident, yielding an upward directed velocity of -160 ± 70 km s^{-1}. Since the blueward component is rather smaller than the one at rest, a single component fitting would yield a lower limit of only ~ -20 km s^{-1} for the upward velocity of the hot flare plasma.

The use of multi component fitting to the Fe XIX 592 profile implies the assumption that the moving structures are smaller than the resolution element. This might seem surprising for spatially resolved observations, since the rest component has long been attributed to the lack of spatial resolution of earlier data, but it appears to be a real feature of the flaring area in this event. Altough we are able to clearly distinguish between the loop legs, where motions are measured, and the loop top, where emission is strong but at rest wavelength, we are not able to resolve the flaring kernel itself, particularly after averaging over 5 CDS pixels.

No detectable Doppler shift were observed in the Fe XVI 360 Å line. However, the post-

recovery line profiles are particularly broad for NIS-1 spectra (308 − 381 Å), thus making impossible to resolve small blueshifted components from the rest profile.

5.2. Flows During the Flare

The most conspicuous effect before the flare impulsive phase is given by the eruption of the filament, readily visible as upwards motions of 10−20 km s^{-1} as measured in the chromospheric lines around 16:00:30 UT, i.e. slightly earlier than the first Neupert peak. Figure 6*a* displays the upwards motions as measured in the He I 10830 Å line, overlaid on the corresponding Hα spectroheliogram. No flows in these positions are measured in the TR or coronal data acquired around 15:57 UT, possibly the AR filament is too "thin" to be visible with the CDS spatial resolution. Also, given its very low emissivity, it would be difficult to measure its shifted component when averaged over the strongly emitting active region. Finally, CDS most probably missed this very short lived phenomenon, since it sampled the area of the filament eruption minutes before (15:57 UT) and after it (16:02:30 UT). The small patch of chromospheric downward velocities visible in Figure 6*a* on the right side of the filament could be the first indication of chromospheric downflows related to the flare start (Ichimoto & Kurokawa 1984) that become more clearly visible in the successive velocity maps.

During the flare initial phase, strong downflows (30-40 km s^{-1}) following the shape of the developing ribbons are measured in He I 10830 in the raster acquired around 16:05 UT. They are shown as black solid contours in Figure 6*b*, overlaid on the same Hα spectroheliogram of Figure 6*a*. Strong upward motions are instead measured in O V around 16:02:30 UT, with values reaching 100 km s^{-1}. Their contours are overlaid as white lines in Figure 6*b*. The same spatial pattern of upward velocities is obtained also in He I 584, although with values a factor two lower. As one can see from Figure 6, the TR upflows and chromospheric downflows are spatially coincident over the area of the maximum O V velocity. This is the same area, $\approx 10''$ wide, where upflows of about −160 km s^{-1} are measured at the same time in the Fe XIX 592 coronal line. This is the first time that quasi-simultaneous and opposite directed motions in different atmospheric layers are observed in the same spatial location during a flare. Given the temporal delay between the CDS and DST measurements with respect to the typical duration of impulsive motions at both coronal and chromospheric levels (30-90 s, Antonucci, 1989; Ichimoto & Kurokawa, 1984), we are most probably not observing the same flaring episode. However, it is well known that during the development of two-ribbon flares magnetic reconnection and its associated effects, such as impulsive flows, occur repeatedly in very close spatial positions (Forbes & Acton, 1996; Falchi, Qiu & Cauzzi, 1997; Czaykowska

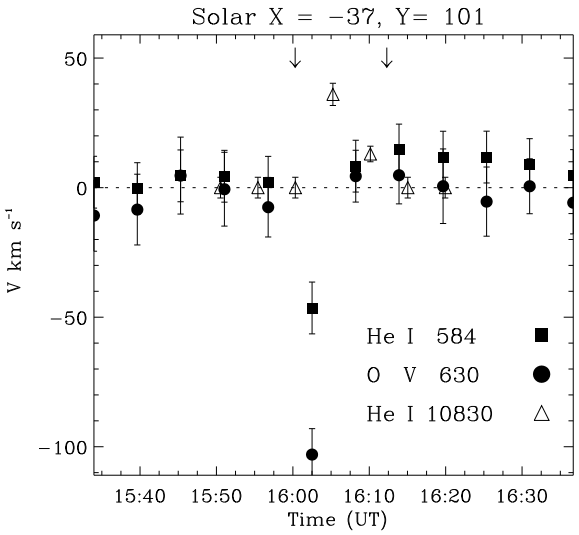

Fig. 7.— Temporal evolution of the observed Doppler shift at the location of maximum blueshift in O v 630 (filled circles). Filled squares represent measurements in the He i 584 Å line while open triangles indicate velocities measured through the He i 10830 Å line. Arrows correspond to the time positions of the main peaks in the time derivative of the SXR curve (see Fig. 1).

et al. 1999), so it seems plausible that we are witnessing distinct events within the same area.

Comparing Figure 6*b* with Figure 3*b*, one sees that the strongest O v (and He i 584) velocities are not cospatial with the flaring loop outlined by the coronal emission. Their pattern rather suggests the presence of adjacent loops at different temperatures, with different inclination with respect to the solar surface, but with footpoints on the same chromospheric area.

The temporal evolution of flows in the location of maximum O v upflow is summarized in Figure 7. One notices that the TR upflows are limited to one single sampling time, while the corresponding chromospheric downflows have a longer duration. The persistence of chromospheric downflows could be due to repeated, elementary episodes occurring in extremely localized kernels at different times, rather than to a continuation of a single episode (Ichimoto & Kurokawa, 1984). The lack of corresponding signatures at TR levels could be due to the non-exact temporal correspondence of the measurements or to a small amplitude of the flows.

Upflows in O v are measured only at one other time (16:13:50 UT, slightly after the

second Neupert peak), in a few pixels around the position (−20, 101), that corresponds to the northern footpoint of loops involved in this second flaring episode. The amplitude of the flows is smaller with respect to the first episode (−30 km s^{-1}), and no clear chromospheric or coronal counterpart is detected. The smaller amplitudes of the flows could be due to an increased atmospheric density induced by earlier episodes of energy release (Doyle et al. 1985; Cauzzi et al. 1995).

6. SUMMARY AND DISCUSSION

We presented simultaneous, spatially and temporally resolved chromospheric, transition region and coronal observations of a small eruptive flare (C1.1 GOES class), throughout its whole development. Spectral rasters were acquired by CDS aboard SOHO and with the HSG at the Dunn Solar Telescope of NSO-Sacramento Peak. This fairly complete dataset allowed us to properly test the model of chromospheric evaporation during flares, by means of a comparison between location, timing, and direction of the plasma motions developing during the flare in different atmospheric layers.

The development of the flare is consistent with the classical picture of two-ribbon events:

A destabilization of the AR filament near its westernmost footpoint seems the primary trigger of the flare. As the filament moves away from the solar surface ($v_{up} \approx -$ 20 km s^{-1}), the overlying, pre-existing magnetic arcade is stretched upward, and conditions arise for reconnection between oppositely-directed magnetic field lines below the filament (Moore & Roumeliotis 1992). Indeed, the first evidence of flare ribbons occurs near the filament western end. Since the filament "re-appears" unaltered after the end of the flare, we suspect that the destabilization affected only a portion of it, much as the cases described in Tang (1986).

Even though the data had been acquired in spectroheliographic mode, without temporal coherence between ground-based and space instruments, we have been able to observe rapidly evolving phenomena and their spatial distribution. We could clearly identify single flaring kernels in both chromospheric and TR signatures, and outline their spatial coincidence during different phases of the flare. As stated before, coronal emission was mostly located between the chromospheric and TR footpoints, and had a much longer evolutionary time than the TR emission. All of the intensity signatures are consistent with a scenario in which the impulsive-phase emission, such as the hard X-rays or TR emission, is closely associated with the primary energy release in the flare, while the thermal phase is an atmospheric response to it (Hudson & Ryan 1995).

Our most relevant result is the measure of strong and co-spatial oppositely directed plasma motions at the onset of the flare: downflows in the chromosphere (30−40 km s^{-1}) and upflows in upper atmospheric layers (~ -50 km s^{-1} in the low TR He I 584 Å line, ~ -100 km s^{-1} in mid TR O V 630 Å line and between ~ -20 and -160 km s^{-1} in the hot Fe XIX 592 Å flare line). For the first time, we demonstrate that such oppositely directed flows originate from the same flaring kernels in different atmospheric layers. These signatures are highly suggestive of the chromospheric evaporation scenario predicted in theoretical models of flares. A further proof could come from the momentum balance between upward coronal and downward chromospheric plasma but, unfortunately, the temporal delay between the coronal and chromospheric measurements of flows casts some doubts on the correctness of such a calculation. If, following the arguments of Sect. 5.2, we assume that the flows measured in roughly the same area at different atmospheric layers can be representative of typical flaring episodes, we can estimate the "instantaneous" upward coronal (P_{up}) and downward chromospheric (P_{down}) momenta (for a definition of P_{up} and P_{down}, see Zarro et al., 1988). Using typical values for the densities in the involved layers, and the measured velocities and volumes, we find that 1.2×10^{19} gr cm $s^{-1} \leq P_{down} \leq 1.2\times10^{20}$ gr cm s^{-1}, while 2×10^{19} g cm $s^{-1} \leq P_{up} \leq 6.9 \times 10^{19}$ g cm s^{-1}. The lower and upper limits for P_{down} derive from the uncertainties in the thickness of the condensations, while for P_{up} they correspond to the two values of coronal upflows measured with the single or double fitting, respectively, and the related changes in emission measure. They seem in rather good agreement, but we remark that the uncertainties in all the parameters needed for the calculation of momenta are such that only order of magnitude estimates are possible.

In the hypothesis of a single flaring loop with a thin ($\sim$ 100 km) transition region, and assuming a continuous flow at TR and coronal levels, we find that the upward momentum of the transition region moving plasma is 1-2 orders of magnitude lower than that calculated in the corona at the same time. However, the O V velocity contours (Fig. 6*b*) point towards a topology different from that suggested by the classical concept of temperature and density stratified loops. The contours seem to indicate the presence of $T_e \sim 10^5$ K loops, whose footpoints lay over the chromospheric ribbons, without an obvious coronal counterpart. We can then argue the presence of adjacent hot ($T_e \geq 10^6$ K) and cool ($T_e \approx 10^5$ K) loops mixed within the chromospheric flaring area. The presence in a magnetic arcade of both hot and cool loops is inferred through theoretical considerations (Antiochos & Noci, 1986; Feldman & Laming, 1994) and validated by recent high resolution observations by SOHO and TRACE (e.g. Brekke 1999), that show how even low temperature plasma outlines full loop structures extending to coronal heights. How this complicated structure is involved in a flare requires complex multistructure models; hydrodynamic simulations of flaring plasma generally refer to plasma confined in a single coronal loop and cannot simultaneously explain

TR and coronal lines (e.g. Betta et al. 2001).

Finally, although powerful enough to drive chromospheric evaporation, the main flare disturbance did not penetrate in deep chromospheric layers. The small total amount of energy released in the event is confirmed by the GOES X-ray classification of C1.1. However, we find it worthwhile to remark that even such small events, when observed with the proper resolution, can reveal a wealth of information.

The work of L.T. has been supported by ASI and MIUR. We thank the staff of the NSO/SP for the generous allocation of observing time at the DST. Particularly warm thanks are due to the DST observers for their precious help during the observing campaign. NSO is operated by AURA, Inc., under cooperative agreement with the NSF. We would also like to thank the CDS team for helping us in planning and obtaining our observations. SOHO is a mission of international cooperation between ESA and NASA.

REFERENCES

Andretta, V., Del Zanna, G., & Jordan, S. D., 2002, submitted to A&A

Andretta, V., & Jones, H. P., 1997, ApJ, 489, 375

Antiochos, S. K., & Noci, G., 1986, ApJ, 301, 440

Antonucci, E., et al., 1982, Solar Phys., 78, 107

Antonucci, E. 1989, Solar Phys., 121, 31

Betta, R. M., Peres, G., Reale, F., & Serio, S., 2001, A&A, 380, 341

Brekke, P., 1999, Solar Phys., 190, 379

Brekke, P., Rottman, G. J., Fontenla, J., & Judge, P. G. 1996, ApJ, 468, 418

Canfield, R. C., Zarro, D. M., Metcalf, T. R., & Lemen, J. R. 1990, ApJ, 348, 333

Cauzzi, G., Falchi, A., Falciani, R., & Smaldone, L. A. Schwartz, R. A., Hagyard, M., 1995, A&A, 299, 611

Cheng, C. C., 1984, Mem. S.A.It., 55, 663

Cheng, C. C. & Tandberg-Hanssen, E. 1986, ApJ, 309, 421

Cheng, C. C, Vanderveen, K., Orwig, L. E., & Tandberg-Hanssen, E., 1988, ApJ, 330, 480.

Culhane, J. L. 1996, Adv. Space Res., vol. 17, no. 4-5, 29

Czaykowska, A., de Pontieu, B., Alexander, D., & Rank, G. 1999, ApJ, 521, L75

Del Zanna, G., Gibson, S. E., Mason, H. E., Pike, C. D. & Mandrini, C. H. 2002, Adv. Space Res., vol. 30, no. 3, 551

Dennis, B., & Zarro, D. M. 1993, Solar Phys., 146, 177

Doschek, G. A., Feldman, U., Kreplin, R. W., & Cohen, L. 1980, ApJ, 239, 725

Doyle, J. G., Byrne, P. B., Dennis, B. R., Poland, A. I., & Emslie, A. G. 1985, Solar Phys., 98, 141

Falchi, A., Falciani, R., & Smaldone, L. A. 1992, A&A, 256, 255

Falchi, A., Qiu, J. & Cauzzi, G. 1997, A&A, 328, 371

Feldman, U. & Laming, J. M. 1994, ApJ, 434, 370

Fisher, G. H., 1986, Lecture Notes in Phys., 255, 53

Fontenla, J. M., Avrett, E. H., & Loeser, R., 1993, ApJ, 406, 319

Forbes, T. G. & Acton, L. W. 1996, ApJ, 459, 330

Gan, W. Q., Zhang, H. Q., & Fang, C. 1991, A&A, 241, 618

Harrison R. A., et al. 1995, Solar Phys., 162, 233

Harrison R. A., et al. 1997, Solar Phys., 170, 123

Hudson, H., & Ryan, J. 1995, ARA&A, 33, 239

Ichimoto K., & Kurokawa K., 1984, Solar Phys., 93, 105

Lites, B. W., Bruner, E. C., Jr., & Wolfson, C. J. 1981, Solar Phys., 69, 373

Mason, H. E., & Bhatia A. K. 1978, MNRAS, 184, 423

Mariska, J. T. 1992, The Solar Transition Region (Cambridge: Cambridge Univ. Press)

Moore, R. L., & Roumeliotis, G. 1992, Lecture Notes in Phys., 399, 69

Nagai, F., & Emslie, A. G. 1984, ApJ, 279, 896

Neupert, W. M., 1968, ApJ, 153, L59

Rilee, M. L., & Doschek, G. A. 2001, ApJ, 554, 464

Scherrer P. H., et al. 1995, Solar Phys., 162, 129

Tang, F. 1986, Solar Phys., 105, 399

Veronig A., et al., 2002, A&A, 392, 699

Woodgate, B. E., Shine, R. A., Poland, A. I., & Orwig, L. E. 1983, ApJ, 265, 530

Wülser, J. P., Zarro, D. M., & Canfield, R. C. 1992, ApJ, 384, 341

Wülser, J. P., et al. 1994, ApJ, 424, 459

Zarro D. M., Canfield R. C., Strong K. T., & Metcalf T. R. 1988, ApJ, 324, 582